UHASSELT
KNOWLEDGE IN ACTION

Maastricht University

# Faculty of Medicine and Life Sciences
## *School for Life Sciences*
## Master of Biomedical Sciences

***Master's thesis***

***Skeletal Responses to Total Body Irradiation and Subsequent Mechanical Loading***

**Bente Van den Broeck**

Thesis presented in fulfillment of the requirements for the degree of Master of Biomedical Sciences, specialization Molecular Mechanisms in Health and Disease

**SUPERVISOR :**
dr. Margarita TEVOSIAN

**SUPERVISOR :**
dr. Cecilia ENGDAHL

**2025**
**2026**

Transnational University Limburg is a unique collaboration of two universities in two countries: the University of Hasselt and Maastricht University.

UHASSELT
KNOWLEDGE IN ACTION

**www.uhasselt.be**
Universiteit Hasselt
Campus Hasselt:
Martelarenlaan 42 | 3500 Hasselt
Campus Diepenbeek:
Agoralaan Gebouw D | 3590 Diepenbeek

# Faculty of Medicine and Life Sciences
## *School for Life Sciences*
Master of Biomedical Sciences


***Master's thesis***

***Skeletal Responses to Total Body Irradiation and Subsequent Mechanical Loading***


**Bente Van den Broeck**


Thesis presented in fulfillment of the requirements for the degree of Master of Biomedical Sciences, specialization Molecular Mechanisms in Health and Disease


**SUPERVISOR :**
dr. Margarita TEVOSIAN

**SUPERVISOR :**
dr. Cecilia ENGDAHL

# Skeletal Responses to Total Body Irradiation and Subsequent Mechanical Loading*

Bente Van den Broeck[1, 3, 4], Margarita Tevosian[2] and Cecilia Engdahl[3, 4]

[1]Hasselt University, Faculty of Medicine and Life Sciences, Campus Diepenbeek, Agoralaan Building D – B-3590 Diepenbeek,
[2]Dynamic Bioimaging Lab, Advanced Optical Microscopy Centre, Biomedical Research Institute, Agoralaan C (BIOMED), Diepenbeek, Belgium.
[3]Department of Rheumatology and Inflammation Research, Sahlgrenska Academy, University of Gothenburg, Gothenburg, Sweden.
[4]Department of Internal Medicine and Clinical Nutrition, Sahlgrenska Osteoporosis Centre and Centre for Bone and Arthritis Research, Institute of Medicine, Sahlgrenska Academy, University of Gothenburg, Gothenburg, Sweden.

*Running title: *TBI effect on skeletal*

To whom correspondence should be addressed: Cecilia Engdahl, Tel: +46 70-889 27 77; Email: cecilia.engdahl@gu.se

**Keywords:** Irradiation, Bone homeostasis, Mechanical loading, Osteoimmunology, Apoptosis

## ABSTRACT

**Radiation therapy is a highly effective cancer treatment, but it is associated with long-term adverse effects on skeletal integrity. While radiation-induced bone loss and increased fracture risk are well documented, the underlying mechanisms remain incompletely understood. Previous *in vitro* findings suggested that osteoclasts may contribute to the clearance of radiation-induced apoptotic cells through efferocytosis, potentially affecting bone homeostasis. Therefore, this study first aimed to explore whether such interactions could also be visualized *in vivo* using an advanced imaging-based approach. To this end, an imaging workflow combining tissue clearing and immunofluorescence was established to assess the co-localization of apoptotic cells and bone-resident cells in murine bone tissue following irradiation. While tissue clearing was successful and apoptotic cells could be detected, further optimization of bone cell-specific immunostaining is required to reliably visualize osteoclast interactions with apoptotic cells *in vivo*. In addition, this study investigated the effects of mechanical loading on irradiated bone and evaluated its potential to improve bone quality following irradiation. Mice were exposed to irradiation and subjected to unilateral tibial mechanical loading at either 2 or 10 weeks post-irradiation. Bone microarchitecture was assessed using micro-computed tomography, while immune alterations were evaluated by flow cytometry and organ weight analysis. Mechanical loading improved trabecular and cortical bone parameters in both control and irradiated mice, demonstrating that the irradiated skeleton retained responsiveness to mechanical loading. These findings highlight mechanical loading as a promising strategy to mitigate radiation-induced skeletal deterioration.**

## INTRODUCTION

Cancer represents a major global health burden and is one of the leading causes of mortality worldwide (1-3). Four conventional treatments, radiation therapy, surgery, chemotherapy, and hormonal therapy, are used to remove cancerous tissue, each with specific advantages and limitations. Approximately half of all cancer patients receive radiation therapy at some point during their treatment course (1, 3). Importantly, cancer survivors who have undergone radiation therapy display an increased risk of bone fractures, highlighting the bone as a clinically relevant site of long-term treatment-related morbidity (4-6). Consequently, a comprehensive understanding of bone biology and the mechanisms underlying radiation therapy-induced skeletal damage is essential for developing strategies that prevent or mitigate these adverse effects and improve long-term patient outcomes. Therefore, this study focuses on radiation therapy and its secondary effects on bone tissue, and whether loading can reverse the decreased bone density that occurs after irradiation.

Bone is a highly specialized connective tissue composed of an organic matrix, primarily cross-linked type I collagen, and a mineral phase dominated by carbonated apatite (7, 8). This composite structure enables bone to fulfill

essential functions, including mechanical support and protection, mineral homeostasis, and hematopoiesis. Skeletal development occurs through intramembranous and endochondral ossification (7).

Structurally, bone is organized into cortical and cancellous compartments with distinct architectural and functional properties (7, 8). Cortical bone forms the dense outer shell of bones and is predominantly located at the diaphysis of long bones, where it provides mechanical strength and load-bearing capacity. In contrast, cancellous bone, also referred to as trabecular or spongy bone, is primarily located in the ends of the long bones and in the vertebrae and consists of an interconnected trabecular network that efficiently distributes mechanical forces to the cortex (7). Bone marrow, housed within these compartments, supports hematopoiesis and gives rise to all immune cells. In adults, it largely consists of adipose-rich yellow marrow. Bone is a highly vascularized tissue, as diffusion alone is insufficient to sustain cellular metabolism within the mineralized matrix.

Bone undergoes continuous renewal through a tightly regulated process known as bone remodeling (8, 9). Remodeling occurs either stochastically or in response to specific stimuli such as microdamage or apoptosis (9, 10). This process is orchestrated by three principal cell types: osteoclasts, osteoblasts, and osteocytes, whose coordinated actions maintain skeletal integrity.

Osteoclasts are the primary bone-resorbing cells and originate from hematopoietic lineage precursors under the stimulation of receptor activator of nuclear factor κB ligand (RANKL) and macrophage colony-stimulating factor 1 (M-CSF) (10, 11). Osteocytes and osteoblasts are important sources of both RANKL and M-CSF and thereby play a central role in osteoclastogenesis. Osteoprotegerin (OPG), produced by osteoblasts and osteocytes, acts as a decoy receptor for RANKL and inhibits osteoclast differentiation. Mature osteoclasts are multinucleated and tartrate-resistant acid phosphatase (TRAP)-positive, and they undergo apoptosis upon completion of their resorptive function or at the end of their lifespan.

Osteoblasts are responsible for bone formation and arise from mesenchymal progenitor cells (8, 10, 11). Their differentiation and activity are regulated by multiple transcriptional programs activated downstream of the bone morphogenetic protein (BMP) and Wnt signaling pathways (10, 11). Osteoblasts synthesize bone matrix proteins and mediate mineralization. Following matrix deposition, osteoblasts may undergo apoptosis, differentiate into bone lining cells that cover quiescent bone surfaces, or become embedded within the matrix as osteocytes.

Osteocytes, which constitute the most abundant bone cell population, are former osteoblasts entrapped within the mineralized matrix (10, 11). They reside in lacunae and extend cytoplasmic dendritic processes through canaliculi, forming an extensive communication network via gap junctions. This lacunar-canalicular system enables the transport of signaling molecules and allows osteocytes to function as mechanosensors. Osteocytes detect fatigue-induced microdamage and repetitive mechanical loading and initiate targeted bone remodeling by signaling to osteoclasts to repair the damage. In addition, osteocytes respond to systemic hormonal cues and contribute to the regulation of both bone formation and resorption.

Bone remodeling proceeds through a series of tightly coupled, sequential phases (9, 10). The process is initiated when osteocytes detect microdamage and emit signals that recruit hematopoietic precursors and stimulate osteoclastogenesis. Bone lining cells subsequently retract, permitting mature osteoclasts to adhere to the mineralized surface.

During the resorption phase, osteoclasts create a sealed acidic microenvironment in which the organic matrix is degraded by proteolytic enzymes (10). This is followed by the reversal phase, during which osteoclasts undergo apoptosis, and pre-osteoblasts are recruited to the resorption site. Osteoblast precursors then differentiate into mature osteoblasts, initiating the formation phase. Osteoblasts deposit an unmineralized collagen-rich matrix known as osteoid, which is subsequently mineralized through the incorporation of calcium and phosphate ions (9). Throughout this phase, inhibitory signals such as OPG are produced to prevent the renewal of osteoclast activation. The remodeling cycle concludes with a resting phase once the resorbed bone has been fully replaced and cellular activity subsides (9, 10).

Mechanical loading is an established *in vivo* experimental approach that stimulates bone

formation in mice (12, 13). Repeated loading induces mechanical strain and fluid flow within the bone matrix, which are sensed by osteocytes and translated into site-specific remodeling signals. Through osteocyte-mediated mechanotransduction, loading promotes osteoblast activation and shifts the remodeling balance toward bone formation. Consequently, mechanical loading increases cortical area, cortical thickness, periosteal circumference, and trabecular bone volume, and has been shown to improve bone mass and microarchitecture under conditions of impaired skeletal homeostasis.

Radiation therapy is a highly effective cancer treatment and is used in combination with cytotoxic drugs to condition patients prior to hematopoietic stem cell transplantation (HSCT) (2, 3, 14). However, conditioning treatment, such as radiation therapy, affects both malignant and healthy tissues, including bone. In addition, bone tissue is particularly vulnerable to radiation exposure due to its high calcium content, active cellular turnover during bone remodeling, and close association with radiosensitive bone marrow with fast-dividing hematopoietic cells (6, 15). Especially, lymphoid and myeloid cells are highly sensitive to irradiation and undergo massive apoptosis after exposure to irradiation (14, 16, 17).

Ionizing radiation induces cellular stress and DNA damage, which can impair cell survival and function. Rather than triggering immediate apoptosis, radiation therapy frequently first induces mitotic catastrophe, a protective mechanism that prevents the proliferation of cells unable to complete mitosis due to extensive damage or checkpoint failure (18, 19). Cells undergoing mitotic catastrophe may subsequently undergo apoptosis, senescence, or necrosis, depending on the cellular context and the severity of the damage.

Within the different types of bone, trabecular and cortical bone exhibit distinct sensitivities to irradiation. Trabecular bone, characterized by higher turnover and greater surface area in contact with bone marrow, is affected at lower radiation doses than cortical bone, which is more resistant to radiation therapy (20, 21). Radiation therapy has been shown to reduce bone mineral density and disrupt bone microarchitecture, thereby contributing to increased fracture risk and long-term morbidity in cancer survivors (4, 5, 22). Some suspect that ionization in the bone marrow microenvironment may activate osteoclasts due to substantial damage (20).

Apoptosis is a tightly regulated form of programmed cell death that plays an essential role in tissue development, homeostasis, and turnover (1, 23, 24). Importantly, apoptosis is also an integral component of normal bone remodeling, in which apoptotic mesenchymal and bone-resident cells initiate osteoclast-mediated bone resorption (9, 10). Following radiation therapy, apoptosis is increased within bone tissue, affecting osteoblasts, osteocytes, and osteoclasts. This increase in apoptotic burden has the potential to disturb local remodeling dynamics by altering cellular communication within the bone microenvironment. Disturbance of the balance between bone resorption and bone formation leads to divergent bone densities.

The clearance of the apoptotic cells occurs through efferocytosis, a highly regulated phagocytic process that is immunosuppressive, promotes tissue repair, and prevents secondary necrosis and inflammation (25-28). Within bone tissue, efferocytosis is carried out by resident phagocytic populations, including macrophages, monocytes, dendritic cells, and, as more recently proposed, osteoclasts themselves (14, 28-30). A recent study by Saghy et al., in the lab of Cecilia Engdahl, examined the co-localization of osteoclasts and osteoclast precursors with apoptotic cells *in vitro*. It was observed that preosteoclasts participated in the efferocytosis of apoptotic cells (14).

Efferocytosis within the bone microenvironment can actively influence local signaling. Clearance of apoptotic cells is associated with the release of anti-inflammatory mediators, including transforming growth factor beta 1 (TGF-β1), which can modulate both osteoclast and osteoblast activity (26, 27, 31). In addition to the suspected effects of apoptosis and efferocytosis, radiation therapy induces immune activation and promotes the release of pro-inflammatory cytokines, including interleukin-1 (IL-1), interleukin-6 (IL-6), and tumor necrosis factor (TNF) (32, 33). These cytokines are potent stimulators of osteoclast differentiation and activity and may further exacerbate bone resorption. Although this inflammatory response is often acute, persistent low-grade inflammation can sustain osteoclast activity and disrupt bone homeostasis over time.

Furthermore, immune and bone cells are closely interconnected through pathways such as the RANKL-RANK-OPG axis, with activated T cells serving as a major source of RANKL and B cells contributing both RANKL and its decoy receptor OPG (34, 35). Radiation therapy alters immune homeostasis by inducing massive apoptosis in hematopoietic and immune cell populations, thereby disrupting the balance between osteoclast and osteoblast stimulation (14).

Together, increased apoptosis, altered efferocytosis, and chronic inflammation may disrupt the balance between bone resorption and formation, leading to reduced bone mass and compromised skeletal integrity following radiation therapy.

The aim of this project was to investigate how radiation therapy-induced cell death affects bone remodeling within the bone microenvironment. Specifically, this study sought to determine the spatial relationship between apoptotic cells and bone-resorbing (pre-)osteoclasts. In addition, this work explored whether mechanical loading, as a physiological stimulus of bone remodeling, can partially restore bone density and microarchitecture following radiation-induced bone loss. By integrating advanced histological imaging approaches, this study seeks to elucidate how apoptosis influences bone remodeling after radiation therapy and to identify potential non-pharmacological strategies to preserve skeletal health in cancer survivors. This is important as cancer survival rates continue to improve and the number of individuals at risk of radiation-induced bone loss is expected to rise. Osteoporotic fractures contribute substantially to premature mortality, chronic disability, and healthcare costs, underscoring the clinical relevance of this research

**EXPERIMENTAL PROCEDURES**

*Mice* – 9-week-old mice were obtained from Janvier Labs and maintained at the Sahlgrenska Academy, Laboratory of Experimental Biomedicine in Gothenburg. All animal procedures complied with the guidelines of the Animal Ethics Committee of Gothenburg (3230–2020). The mice were co-housed in standard cages, kept at 22°C, and exposed to a 12-hour light-dark cycle. They had free access to Teklad Diet 2016 (Envigo, Indianapolis, IN, USA) and tap water. Starting one week before irradiation and continuing for up to 2 weeks post-irradiation, control and irradiated mice received Enrofloxacin (0.6mg/ml, Elanco Denmark ApS), an antibiotic, in their drinking water. During the experiments and before euthanasia, the body weights of the mice were recorded. Mice were anesthetized with Ketador/Dexdomitor (Richter Pharma/Orion Pharma), bled from the axillary vein, and euthanasia was performed via cervical dislocation. Blood, tibia, and femur were collected for further analysis

*Irradiation* – For the acute investigation of irradiation effects, a lethal dose of 9 Gy of total-body X-ray irradiation was administered to the mice to assess effects at 24h and 48h. In the long-term investigation, the mice were irradiated with 9 Gy in two fractions of 4.5 Gy each, with a 4-h interval between fractions, followed by HCST on the same day to assess the effect 2 weeks post-irradiation. The same protocol, two fractions followed by HCST on the same day, was used for the mechanical loading experiments.

*Hematopoietic stem cell transplantation (HSCT)* - Bone marrow cells were harvested from sibling donor mice using the Negative Selection EasySep Mouse Hematopoietic Progenitor Cell Isolation Kit (StemCell), following the manufacturer's instructions. A total of 800,000 enriched HSCs were resuspended in PBS and intravenously injected into the tail vein of irradiated recipient mice, while non-irradiated naive mice received PBS. This procedure demonstrated successful allogeneic bone marrow transplantation in previous work of Engdahl's research group (14).

*Loading* – At 2 weeks or 10 weeks post-irradiation, mice underwent 6 loading sessions. A load of 13N (early loading) or 12N (late loading) was applied to the left tibia using loading equipment (3100 Electroforce test instrument, Bose Corporation, currently available at TA Instruments) under the influence of anesthesia with isoflurane (Baxter Medical AB, Kista, Sweden). Forty cycles/day of compressive load were applied with a rest period of 10 seconds between each cycle in a trapezoidal wave form on seven days. Mice were euthanized, and blood, liver, spleen, thymus, uterus, humerus, tibia, and femur were collected for further analysis. The organs were weighed directly after collection.

*Flow cytometry* - To prepare cells for flow cytometry analysis, bone marrow cells were

flushed out and harvested from the humerus bone using a 25 G syringe with PBS. Following isolation, cells were maintained on ice throughout the procedure unless otherwise stated. The total number of cells was determined using a cell counter (Sysmex, Europe GmBH, Norderstedt, Germany). Cells were plated into 96-well V-bottom plates ($1 \times 10^6$ cells/well) and were centrifuged (1200 rpm, 3 min, 4 °C), after which the supernatant was discarded, and the cell pellet was gently resuspended by vortexing. To prevent nonspecific antibody binding, cells were incubated with an Fc receptor-blocking solution (1:100 dilution in FACS buffer) for 5 minutes at room temperature. Fluorochrome-conjugated antibodies (Suppl table 1) diluted in FACS buffer were added directly to the cells. Samples were incubated (20 minutes, 4 °C) in the dark. Following incubation, FACS buffer was added to each well, and cells were centrifuged again (1200 rpm, 3 min, 4 °C). The supernatant was discarded, and the cells were gently resuspended. This washing step was repeated once more. Finally, cells were resuspended in FACS buffer and transferred to a flow cytometry-compatible plate. Flow cytometry analyses were performed using FACSVerse (Becton Dickinson) and FlowJo (version 10.6.2). Gating was based on the FMO samples (Suppl fig. 1).

*Murine serum analysis* – Serum was collected after centrifugation of the blood (10 min, 9000 rpm, 19°C). Enzyme-linked immunosorbent assays (ELISAs) were conducted to quantify C-terminal collagen type-1 cross-links (CTX-I) (Immunodiagnostic Systems, East Boldon, UK), procollagen type I N pro-peptide (PINP) (Immunodiagnostic Systems), immune cytokine TGF-β1 (Invitrogen), and B cell activating factor (BAFF). Supplemented protocols were followed.

*Micro-computed tomography (µCT)* - To determine periarticular trabecular and cortical bone loss, the proximal metaphyseal areas of the tibiae were scanned by µCT (viva40 CT, Scanco Medical, Brüttisellen, Switzerland). The following measurement settings were used: Voltage, 40kV; X-ray current, 250µA; exposure time, 5000ms/projection for 720 projections; matrix, 1024×1024; voxel size in reconstructed image, 9µm. The following microstructural and density parameters were investigated: trabecular bone volume over total volume (BV/TV), trabecular number (Tb.N), trabecular thickness (Tb.Th), cortical area (Crt. Ar) and, cortical thickness (Crt.Th)

*Histological preparation* – iDISCO+ tissue clearing with modifications performed (36). Bone samples were fixed in PFA (4%, 48 h, 4°C). Following fixation, samples were dehydrated through a graded methanol series (20%, 40%, and 60% methanol (MeOH), 1 h per step, 4°C), followed by incubation in 70% MeOH supplemented with 3% hydrogen peroxide ($H_2O_2$) and 20% dimethyl sulfoxide (DMSO) overnight at 4°C. Samples were further dehydrated in 80% and 100% MeOH (1 h per step, 4°C). For delipidation, samples were incubated in dichloromethane (DCM) (2x 1h + 1x overnight + 2x 2h + 1x overnight, room temperature). Samples were then rehydrated using a reverse MeOH gradient (100%, 80%, and 40% MeOH; 1 h per step, 4°C) and transferred to 2× saline-sodium citrate buffer containing Tween-20 (2× SSC-T) (1h, 4°C). Decalcification was performed in 10% ethylenediaminetetraacetic acid (EDTA) overnight at room temperature, followed by two washes in 2× SSC-T for 1 h each. Following decalcification, samples were incubated in permeabilization buffer (PBS containing 0.2% Triton X-100, 0.1% sodium deoxycholate, 10% DMSO, and 25 mM EDTA, pH 8.0) overnight at room temperature. Then, samples were blocked in staining buffer (PBS/DEPC supplemented with 0.2% Triton X-100, 25 mM EDTA, 10% DMSO, heparin (5 µg/mL), and 5% donkey serum for at least 6 h at room temperature.

*2D imaging* - Samples were cryoprotected in 30% sucrose overnight at 4°C and embedded in optimal cutting temperature (OCT) compound for at least 3h at −20°C prior to sectioning. Tissue sections were washed in PBS-Tween (PBST) for approximately 5 min and air-dried before incubation with primary antibodies (suppl. table 2) overnight at 4°C. Following washing in PBST (5 min), sections were incubated with secondary antibodies (suppl table 2) for 1.5 h at room temperature. After a final PBST wash, nuclei were stained with Hoechst (Invitrogen), and coverslips were placed. Images were made with the Nikon Eclipse Ti2 microscope.

*3D imaging* – Whole-mount samples were incubated with primary antibodies (suppl table 2) for 48 h at 37°C, followed by washing in PBS containing 0.1% Tween-20 and 12.5 mM EDTA (3x 1h, 1x 6 h, 1x overnight wash, at

37°C). Samples were then incubated with secondary antibodies (48h, 37°C) (suppl table 2), followed by the same washing procedure. Nuclear staining was performed by overnight incubation with YO-PRO (1:1000 in PBS-Tween/12.5 mM EDTA) at 37°C. For final clearing, samples were dehydrated in a graded MeOH series (20%, 40%, and 60% MeOH for 1 h each at room temperature), followed by 80% MeOH overnight, 100% MeOH for 1h, overnight incubation in fresh 100% MeOH, and a final 1h incubation in 100% MeOH. Samples were then incubated in DCM twice for 15 min at room temperature and transferred to dibenzyl ether (DBE) for 1 h. Samples were stored in DBE until imaging and imaged within 1-2 days. Images were made with UltraMicroscope Blaze™ (Miltenyi Biotec). ImarisViewer 11.0.0 was used to view both 3D and 2D images.

*Statistics* - All statistical analyses were conducted using GraphPad Prism software (GraphPad Software Inc., La Jolla, CA, USA). Outliers were identified using the ROUT method (Q = 1%) and excluded from the analysis. Two-sided unpaired t-tests with Welch's correction were used to assess statistical differences between two independent groups (control and irradiated). Bone microarchitecture parameters were analyzed using a two-way repeated measures ANOVA, with mechanical loading (loaded vs. non-loaded) as a within-subject factor and irradiation (control vs. irradiated) as a between-subject factor. Post hoc multiple comparisons were performed using Fisher's LSD. Figures showing data mean ± standard deviation (SD), and significance is indicated as follows: *$p < 0.05$, **$p < 0.01$, ***$p < 0.001$, and ****$p<0.0001$.

**RESULTS**

To investigate the potential *in vivo* interaction between radiation-induced apoptotic cells and bone-resident cells, a three-dimensional (3D) microscopy workflow was established to visualize intact bone tissue. As part of this workflow, a tissue clearing protocol was successfully implemented, resulting in substantial optical clearing of the bone samples, as demonstrated by the increased transparency of the tissue after processing (Fig. 1A and 1B).

Following clearing and staining, 3D imaging of the samples was performed. Although image acquisition was successful and structural visualization of the tissue was achieved, the fluorescent signal was dominated by strong bone autofluorescence (Fig. 1C). This substantially hindered the interpretation of the staining patterns and prevented reliable discrimination between specific fluorescence signals and background autofluorescence. As a result, it was not possible to confidently verify the specificity of either the TRAP or cleaved caspase-3 staining in the 3D images. Therefore, we took a step back and evaluated antibody performance in two-dimensional (2D) frozen sections. The staining of cleaved caspase-3 successfully identified apoptotic cells within the bone tissue (Fig. 1D and 1E). Furthermore, the CD45/B220 staining for B cells confirmed preservation of tissue integrity and accessibility of target epitopes (Suppl. Fig. 2A and 2B). The stainings for osteoclast markers Cathepsin K and TRAP, as well as osteoblast markers SP7 and NCAM, did not yield reproducible or specific staining patterns under the tested conditions. Additional antigen retrieval was performed in an attempt to improve signal detection. However, this resulted in substantial tissue damage.

Furthermore, the effects of mechanical loading in mice that underwent irradiation followed by hematopoietic stem cell transplantation were examined and compared with age-matched littermate naïve control mice that did not receive irradiation. The effect of unilateral mechanical loading was examined at two different timings. The first experimental setup received early mechanical loading cycles 2 weeks after irradiation and HSCT. The second experimental setup underwent late mechanical loading, 10 weeks after irradiation and HSCT. In both experimental setups, irradiated animals exhibited significant weight loss, which returned to control levels after a few days of recovery (Fig. 2A and 2B). After the start of the loading cycles, the body weight in the irradiated mice in both experimental setups drops again. A significant difference in body weight was observed at the end of both experiments (Fig. 2C). Furthermore, the weights of several organs were measured and analyzed. The weight of the uterus and thymus was significantly reduced in both the early-loaded irradiated and late-loaded irradiated mice (Fig. 2D and 2E). The spleen weight was increased in early-loaded irradiated mice compared to control mice, but no difference was observed in the late-loaded experimental setup (Fig. 2F). The liver weight remained unaffected (Fig. 2G). A flow

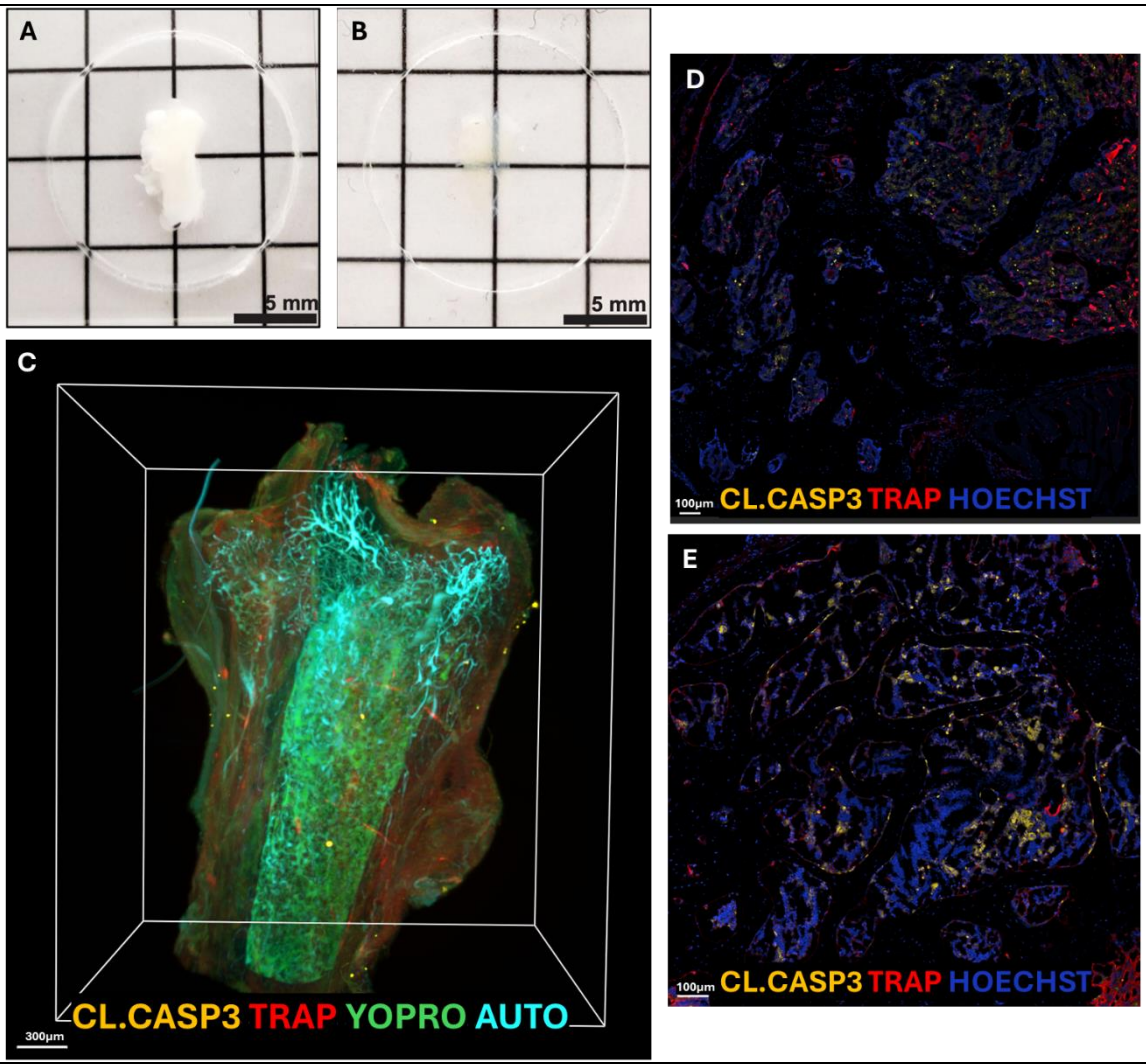


**Figure 1: Representative 2D and 3D images of the bone after irradiation. A** Murine bone before the clearing process. **B** The same murine bone after the clearing process. **C** A 3D image of the femur of an irradiated mouse sacrificed two weeks after irradiation, stained for cleaved caspase 3 (apoptotic cells, yellow), TRAP (osteoclasts, red), and YOPRO (nucleus, green). **D** A 2D image of the growth plate of the tibia of a control mouse sacrificed 48h after irradiation, stained for cleaved caspase 3 (apoptotic cells, yellow), TRAP (osteoclasts, red), and Hoechst (nucleus, blue). **E** A 2D image of the growth plate of the tibia of an irradiated mouse sacrificed 48h after irradiation, stained for cleaved caspase 3 (apoptotic cells, yellow), TRAP (osteoclasts, red), and Hoechst (nucleus, blue).

cytometry analysis of the bone marrow of the humerus was performed to examine the immune cell population present in the bone marrow. Prior to analyzing immune cell frequencies, total bone marrow cellularity was assessed to control for potential bias introduced by differences in total cell numbers between groups. Bone marrow cellularity was comparable between groups at 4 weeks and increased at 12 weeks in irradiated mice (Fig. 3A). Therefore, frequencies are reported, as they reflect the relative composition of the immune compartment and allow detection of changes in specific populations independent of variations in cell yield. The frequency of the $CD19^+$ B cell populations was increased at 12 weeks in the late-loaded irradiated mice (Fig. 3B). No difference was found in the early-loaded experimental setup. In the early-loaded experimental setup, a significant decrease in the frequency of the $CD3^+$ T cell population was observed in the irradiated group (Fig. 3C). The frequency of $F480^+$ macrophages remained unchanged in both experimental setups (Fig. 3D). At last, the neutrophil frequency remained unaffected in the early-loaded experiments however, a decrease was observed at 12 weeks in the late-loaded irradiated mice compared to their controls (Fig 3E).

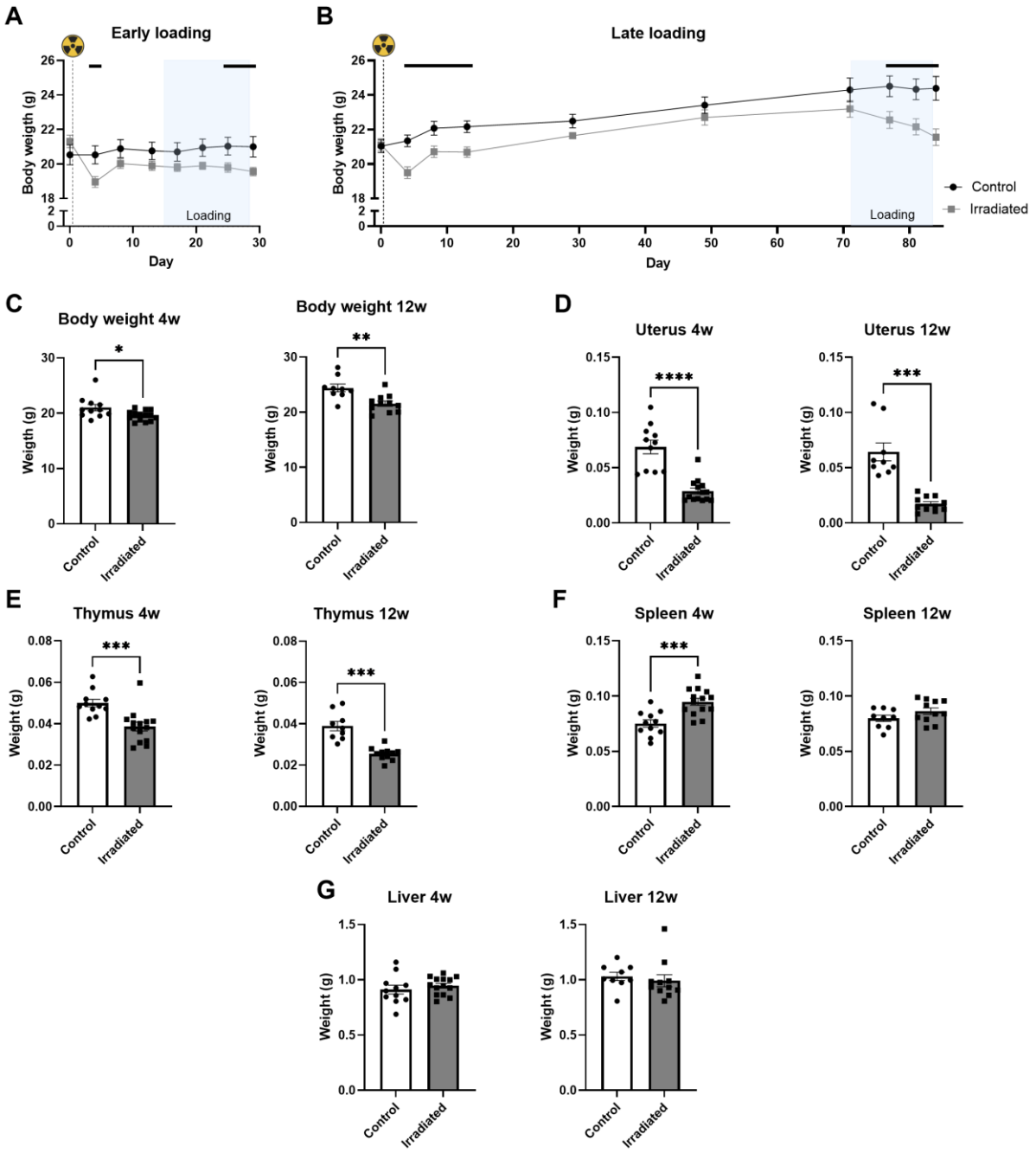


**Figure 2: Analysis of the body and organ weight following mechanical loading.** **A** Representation of body weight fluctuations during the experiment, where the loading was performed after 2 weeks of recovery from the irradiation and HSCT. **B** Representation of body weight fluctuations during the experiment, where the loading was performed after 10 weeks of recovery from the irradiation and HSCT. **A-B** Black line above the graph means a significant difference between the control and irradiated group at that specific time point. **C** Body weight of the mice at the end of the experiments. **D** Uterine weight **E** Thymic weight **F** Splenic weight **G** Liver weight. Statistical analysis involved a two-sided unpaired t-test with Welch's correction. Data are presented as mean (n = 9-14) ± SD, and significance is indicated as *$p < 0.05$, **$p < 0.01$, ***$p < 0.001$, and ****$p<0.0001$ compared to the control group.

B cell activating factor (BAFF) levels were measured because a difference in B cell frequency was detected. BAFF levels were significantly increased in the irradiated group at both time points (Fig. 4A). Furthermore, TGF-β1 levels were examined, as previous work by Engdahl's group showed that it could be an important cytokine associated with radiation-induced bone loss (14). In these experiments, no

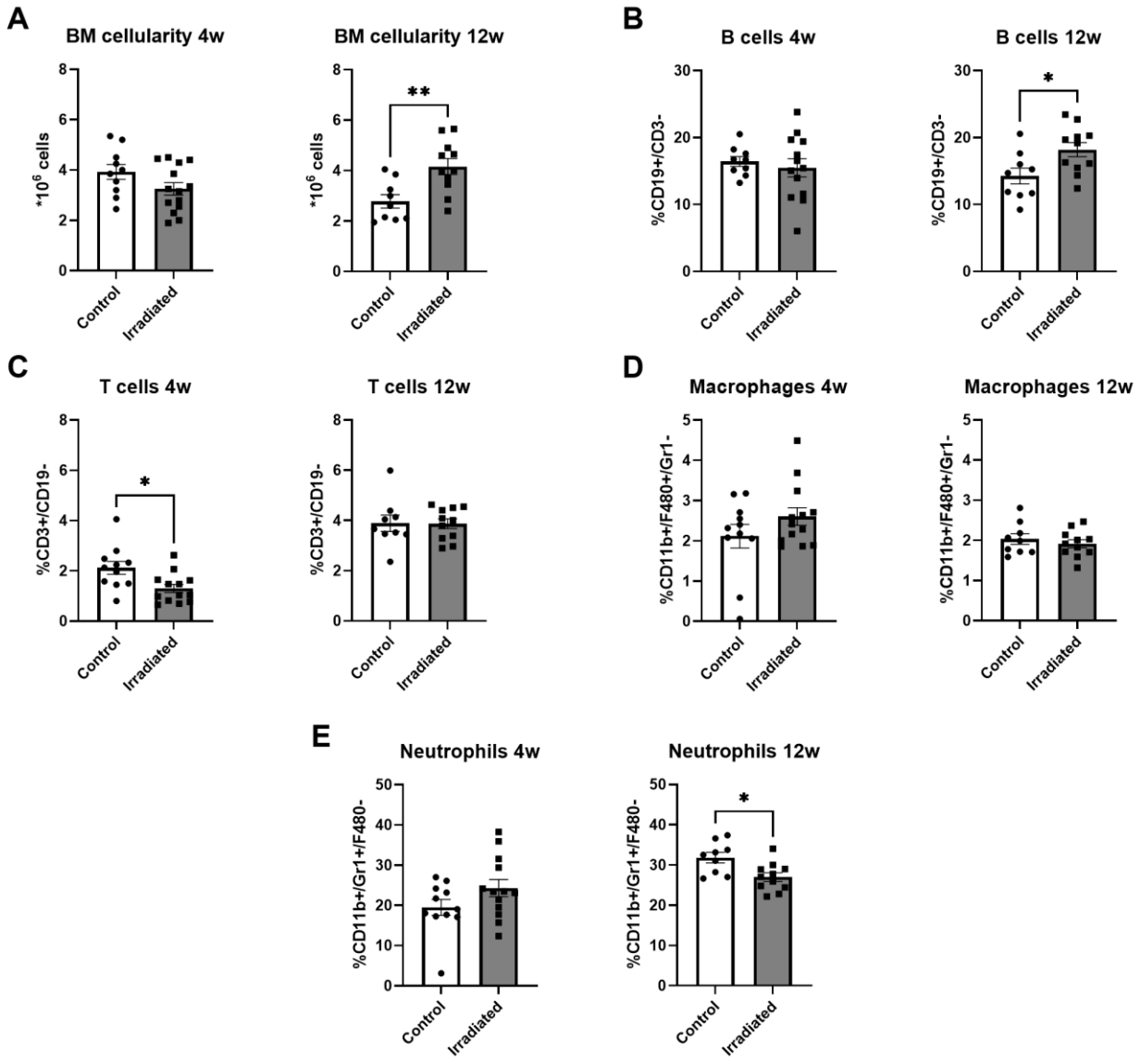


**Figure 3: Analysis of the FACS results from the bone marrow of the humerus after early and late loading. A** Obtained amount of cells from the bone marrow of the humerus **B** Percentage of $CD19^+$ B cells gated on the $CD3^-$ cell population **C** Percentage of $CD3^+$ T cells gated on the $CD19^-$ cell population **D** Percentage of $F480^+$ macrophages gated from the $CD3^-CD11b^+$ cell population **E** Percentage of $Gr1^+$ neutrophils gated from the $CD3^-CD11b^+$ cell population. Statistical analysis involved a two-sided unpaired t-test with Welch's correction. Data are presented as mean (n = 9-14) ± SD, and significance is indicated as $*p < 0.05$ and $**p < 0.01$ compared to the control group.

significant differences in TGF-β1 levels were found (Fig. 4B).

Micro-computed tomography (µCT) was performed at 4 and 12 weeks to measure several trabecular and cortical parameters to evaluate the effects of irradiation on the bone structure, as well as the mechanical loading that was performed on one side. For trabecular bone volume per tissue volume (BV/TV), no significant interaction between mechanical loading and irradiation was observed at either time point (Fig. 5A). However, significant main effects of both loading and irradiation were detected. Mechanical loading increased BV/TV, whereas irradiated mice exhibited overall lower BV/TV values than controls. Post hoc analyses confirmed significant differences between loaded and non-loaded limbs, as well as between control and irradiated groups. The absolute amount of increase in BV/TV is similar in both control and irradiated groups and seems, in general, lower in the late loading (Suppl fig. 3).

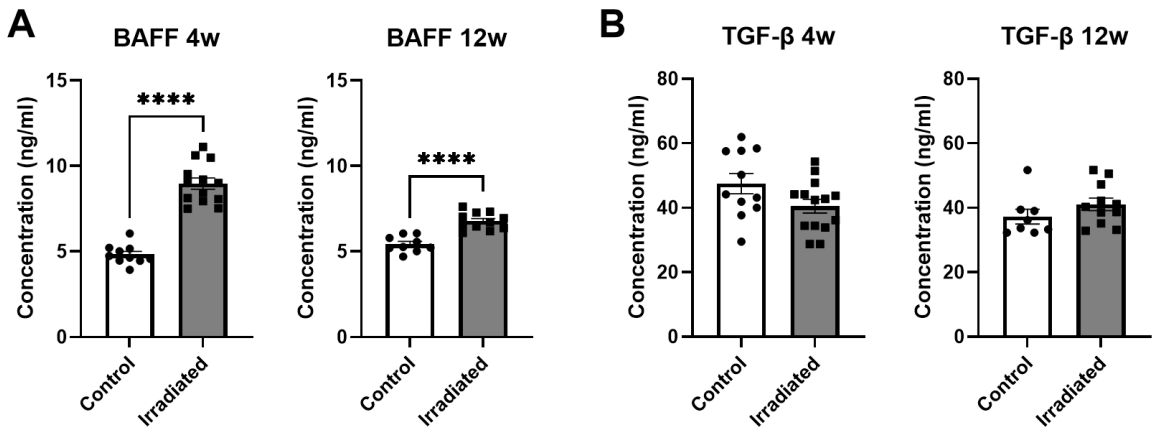


**Figure 4: Effects of irradiation and mechanical loading on B cell activating factor (BAFF) and transforming growth factor beta 1 (TGF-β), and bone formation and absorption markers. A** Serum levels of BAFF. **B** Serum levels of TGF-β. Statistical analysis involved a two-sided unpaired t-test with Welch's correction. Data are presented as mean (n = 8-14) ± SD, and significance is indicated as *p < 0.05 and ****p<0.0001 compared to the control group.

The effects observed in BV/TV are supported by the changes in the different trabecular parameters. The trabecular number (Tb. N) followed the BV/TV pattern (Fig. 5B). Irradiation lowered the Tb. N in general. At 4 weeks, loading increased Tb. N in both control and irradiated mice. At 12 weeks, the loading-induced increase in Tb. N was no longer observed in irradiated mice. For the Tb. N, a significant interaction was detected, indicating a change in response to mechanical loading after irradiation at both time points. Trabecular separation (Tb.Sp), which is inversely related to BV/TV, was increased in irradiated mice compared to controls and reduced by mechanical loading in both groups at 4 weeks (Fig. 5C). A significant interaction between loading and irradiation was observed at this time point, indicating that the response to loading differed between groups. At 12 weeks, no significant interaction was detected, although the main effects of both loading and irradiation remained significant. While loading significantly reduced Tb.Sp in control mice, this effect was no longer observed in irradiated mice. The trabecular thickness (Tb. Th) follows the positive effect mediated by loading, but not the reduction mediated by irradiation (Fig. 5D). Trabecular thickness (Tb.Th) was significantly affected by both irradiation and mechanical loading at 4 weeks (Fig. 5D). Mechanical loading increased Tb.Th in both groups, while irradiated mice exhibited higher Tb.Th values in the loaded bone compared to controls. No significant interaction between irradiation and loading was observed. At 12 weeks, a significant main effect of loading persisted, whereas no significant effect of irradiation was detected. Although no interaction was observed, post hoc analysis revealed that loading significantly increased Tb.Th in irradiated mice, while no significant loading-induced increase was detected in control mice. Cortical parameters showed a more consistent response to loading. For cortical area (Crt. Ar), no interaction or main effect of irradiation was observed at either time point, while loading showed a significant effect, confirmed by the post hoc analyses, where Crt. Ar is increased in both control and irradiated mice after loading (Fig. 5E). Cortical thickness (Crt. Th) followed the same pattern (Fig. 5F). On top of that, the Crt. Th showed a significant decrease in Crt. Th at 4 weeks in the non-loaded irradiated bone compared to the control.

Radiation therapy is known to induce bone loss, whereas mechanical loading induces bone formation. This was also confirmed by our results (Fig. 5). Therefore, serum levels of PINP, a bone formation marker, and CTX-I, a bone resorption marker, were measured. PINP levels were significantly higher in the irradiated group than in the control group at 12 weeks. In contrast, no significant difference was observed between the experimental groups at 4 weeks (Fig. 6A). No significant difference in CTX-I was observed in either experimental setup (Fig. 6B).

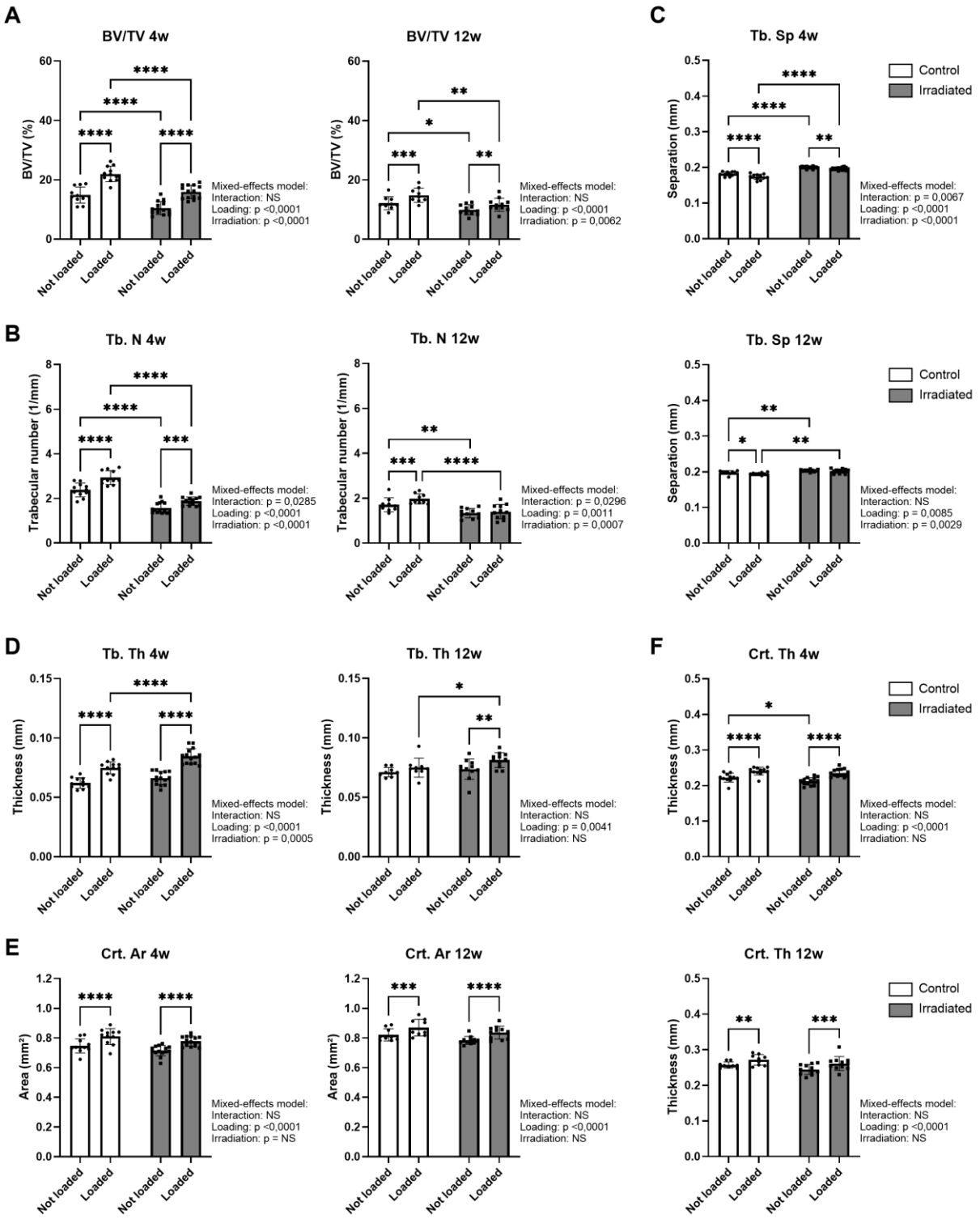


**Figure 5: Mechanical loading improves bone microarchitectural parameters. A** Micro-computed tomography (µCT) analysis of trabecular bone volume per total volume (BV/TV) in the tibia. **B** µCT analysis of trabecular thickness (Tb. Th). **C** µCT analysis of trabecular number (Tb. N). **D** µCT analysis of trabecular separation (Tb. Sp). **E** µCT analysis of cortical area (Crt. Ar). **F** µCT analysis of cortical thickness (Crt. Th). Statistical analysis involved a two-way repeated measures ANOVA, with mechanical loading (loaded vs. non-loaded) as a within-subject factor and irradiation (control vs. irradiated) as a between-subject factor. Post hoc multiple comparisons were performed using Fisher's LSD. Figures showing data mean (n = 9-14) ± SD, and significance is indicated as follows: *p < 0.05, **p < 0.01, ***p < 0.001, and ****p<0.0001.

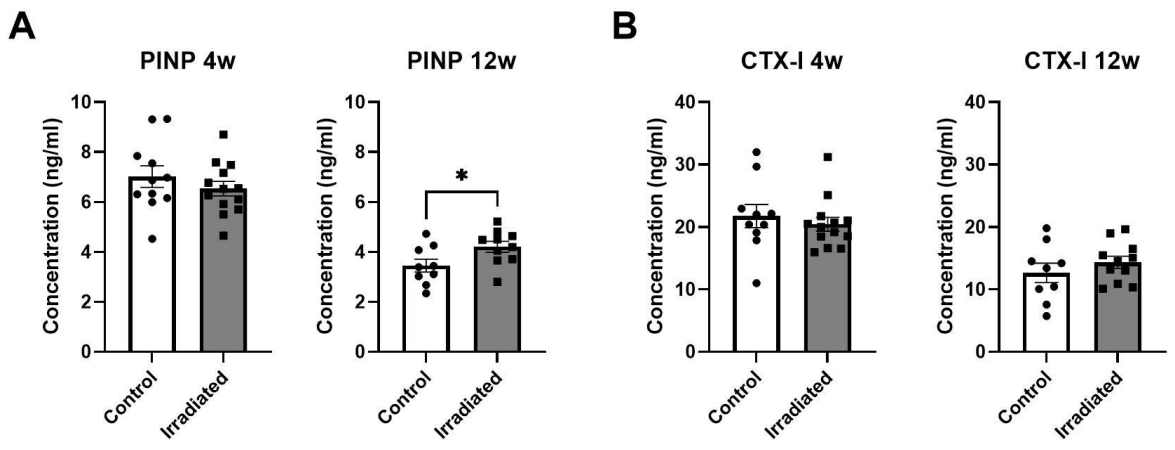


**Figure 6: Effects of irradiation and mechanical loading bone formation and absorption markers. A** Serum levels of procollagen type I N-terminal propeptide (PINP), a bone formation marker **B** Serum levels of C-terminal collagen type-1 cross-links (CTX-I), a bone resorption marker. Statistical analysis involved a two-sided unpaired t-test with Welch's correction. Data are presented as mean (n = 9-13) ± SD, and significance is indicated as *p < 0.05 and ****p<0.0001 compared to the control group..

**DISCUSSION**

Irradiation is known to profoundly disrupt bone homeostasis, affecting both the bone microenvironment and the balance between bone formation and resorption, ultimately leading to decreased bone density (14, 37). These radiation-induced skeletal alterations can have important long-term consequences for cancer survivors, including an increased risk of fractures and reduced bone quality. The exact underlying processes remain incompletely understood. However, recently, Guliyeva G. et al. demonstrated that apoptotic cells can stimulate osteoclastogenesis. Apoptotic cells are a source of AnnexinA1 and can stimulate the AnnexinA1-Dectin-1 axis, a regulator of osteoclastogenesis, thereby inducing bone loss (38). Therefore, apoptotic cells play an important role in the irradiation-induced bone loss.

Previous work by Sághy T. et al. demonstrated that, *in vitro*, (pre-)osteoclasts can engulf apoptotic cells via efferocytosis (14). Building on these previous findings, the present study aimed to investigate whether this interaction and possible engulfment process by (pre-)osteoclasts can also be observed *in vivo*. To this end, a 3D microscopy approach was initially attempted to visualize interactions between osteoclasts and apoptotic cells within the bone microenvironment. However, due to technical limitations, this approach proved challenging. Therefore, a transition was made to a 2D histological approach to identify and optimize suitable antibodies for future application in the 3D approach.

A major challenge in this study was establishing a robust imaging workflow to assess potential *in vivo* interactions between apoptotic cells and bone-resident cells following irradiation. Although the tissue clearing protocol was successful and enabled optical visualization of intact bone structures, the high autofluorescence of mineralized bone tissue substantially compromised signal specificity, making it difficult to distinguish the true signal. Bone autofluorescence is a well-recognized limitation in fluorescence-based imaging of calcified tissues and can obscure low-abundance targets (39, 40). Unfortunately, we were unable to find staining methods that effectively visualized osteoblasts and osteoclasts in our experimental setting.

The successful detection of cleaved caspase-3 and B220 in 2D sections confirmed that tissue preservation and antibody penetration were not universally impaired, suggesting that the unsuccessful osteoclast and osteoblast stainings were more likely related to marker-specific technical limitations rather than general tissue processing failure. This may reflect limited epitope accessibility, insufficient antibody compatibility with frozen bone sections, or inadequate antigen preservation after fixation and decalcification. An attempt was made to improve antigen accessibility by performing antigen retrieval with citrate buffer. However, this process damaged the tissue

sections and could therefore not be incorporated into the workflow going forward.

Future optimization should focus on identifying more robust bone-cell-specific markers and on integrating autofluorescence-quenching protocols in the workflow. In addition, alternative imaging modalities or reporter-based mouse models may provide a more reliable strategy to study *in vivo* osteoclast-mediated efferocytosis in the irradiated bone microenvironment.

In the second part, the effect of mechanical loading after irradiation was assessed, as previous studies have shown that irradiation reduces bone density (4, 14) and that mechanical loading increases bone density (12, 13). Consistent with previous studies, irradiation induced an initial body weight loss, followed by a gradual recovery to a weight almost equal to that of the control group (14). After the start of mechanical loading, the irradiated mice again began to lose body weight, resulting in significantly lower body weight than the control group at the end, whereas the control mice remained at a similar weight. This holds for both the early- and late-loading experimental setups. I think that the weight loss is a consequence of a combination of the prior stress the mice experienced during irradiation, the anesthesia they received on each loading day, and the mechanical loading. Exposure to irradiation can induce metabolic changes (38, 39), making these mice more vulnerable during subsequent tests and stress. Furthermore, previous studies have shown that post-anesthetic weight loss can persist for up to 48 hours in rodents (41) and that postsurgical body weight loss after an anesthetic mixture is due to distress unrelated to pain (42). At last, acute stress can bidirectionally affect feeding behavior, but it is most commonly associated with decreased food intake in animal models (43, 44).

When examining organ weight after collection, overall similar trends were observed in the previous work by Sághy T. et al. (14). At both time points, uterine weight is significantly reduced in irradiated mice. Previous studies support our findings, showing that histological examination of irradiated uteruses also revealed an atrophic myometrium with fibrosis on the serosal surface (45, 46). Furthermore, the endometrium was atrophic, with thickened, smaller blood vessels. The smaller uterus can be related to the irradiation damage and/or hormonal depletion due to associated ovarian failure after irradiation.

The thymus weight was significantly reduced in irradiated mice at both time points. At 12 weeks, the weight of the thymus seems to be, in general, lower than at 4 weeks. It is well established that irradiation and aging cause thymic atrophy, mainly due to stromal cell depletion, which explains our results (47-49). In previous studies, the thymus returned to its normal weight a few weeks after irradiation (14, 50). However, when we continue to stress the mice during mechanical loading, this stress may affect the recovery. The reduction in T cell frequency observed at 4 weeks is most likely a direct consequence of radiation-induced lymphodepletion and bone marrow damage, which impairs the production of T cell progenitors (51). Thymic atrophy may contribute to impaired T cell regeneration, but T cell numbers recovered at later time points despite persistent thymic atrophy. This is consistent with previous studies showing that T cell numbers can be restored after irradiation combined with HSCT achieved through *de novo* production in the thymus, particularly for CD4+ T cells, or homeostatic expansion of peripheral T cells, preferentially for CD8+ T cells (52-54).

Spleen weight increased at 4 weeks in the irradiated mice. However, the spleen weight was not significantly different from that of the control group at 12 weeks. The increase in spleen weight observed following irradiation is likely explained by extramedullary hematopoiesis (EMH), a well-established compensatory response to bone marrow damage (55). As bone marrow function recovers over time, the need for EMH diminishes, leading to normalization of spleen weight.

Upon further analysis of the humeral bone marrow immune cell population, B cell frequency was elevated at 12 weeks in irradiated mice compared to the control group. This elevation is likely due to an overcompensation for the massive B cell apoptosis following irradiation, as B cells are the most radiosensitive lymphocytes and are almost completely depleted after irradiation (14, 17). One potential stimulator of B cell formation may be B cell-activating factor (BAFF), a critical cytokine involved in B cell survival, maturation, and homeostasis that signals through the BAFF receptor (BAFFR) (56). In the present study, elevated systemic BAFF levels were observed in irradiated mice

at both time points, suggesting persistent alterations in B cell regulatory signaling following irradiation and mechanical loading. Interestingly, BAFF levels seemed to be higher at 4 weeks than at 12 weeks, whereas increased B cell frequency was observed only at the later time point. I think BAFF levels are declining because the B cell population recovers by 4 weeks after radiation treatment, but the overall process is delayed. These findings are in line with the previous study by Sághy et al., which also reported elevated BAFF levels at 12 weeks following irradiation alone, although no increase in B cell frequency was observed at that time point (14).

On the other hand, the neutrophil cell frequency is decreased at 12 weeks in the irradiated group. In literature, it is stated that radiation therapy can cause neutropenia as radiation therapy depletes precursor cells (57, 58). However, since the mice received an HSCT, it is expected that sufficient precursor cells were provided. The study by Sághy T. et al. also showed that the neutrophil population was restored at 12 weeks post radiation therapy (14).

TGF-β1 was measured without any differences between the control and irradiated groups. It was suspected that TGF-β could be elevated as TGF-β1 production is increased after irradiation and during efferocytosis (27, 31). Furthermore, recent work by Sághy T. et al. described this and further investigated the role of TGF-β1 (14). They demonstrated that TGF-β1 partially mediates the effect of apoptotic cells on bone marrow monocytes differentiating toward osteoclasts *in vitro*, suggesting a mechanistic link between apoptosis, efferocytosis, and enhanced bone resorption following irradiation.

Furthermore, load-bearing exercise is widely recognized as a key regulator of bone architecture and strength and is therefore commonly recommended to maintain bone quality in all individuals (12, 13). Previous studies have shown that patients undergoing radiation therapy exhibit an increased risk of fractures, largely attributed to radiation-induced reductions in bone density (4-6). Therefore, the present study investigated the potential of mechanical loading to restore bone structure following irradiation. µCT was used to assess the structural effects of irradiation and loading on one tibia from each control and irradiated mouse. Overall, mechanical loading consistently improved trabecular and cortical bone parameters. For most bone parameters, no interaction effects between irradiation and mechanical loading were observed, suggesting that the effects of irradiation and mechanical loading were largely independent rather than synergistic or antagonistic. Irradiation significantly affected trabecular bone parameters except the trabecular thickness. This is in line with what Sághy T. et al. have reported. These findings suggest that radiation-induced trabecular bone loss is predominantly caused by the loss of individual trabeculae rather than the thinning of existing trabeculae. Irradiation did not appear to significantly affect cortical bone parameters. In a previous study by Sághy T. et al., a reduction in cortical thickness following irradiation was observed (14). However, this was not observed in our study. In general, cortical bone is less sensitive to irradiation than trabecular bone, as trabecular bone is characterized by higher turnover and greater surface area in contact with bone marrow (20, 21). The effect of loading was significant in all the bone parameters. Both the trabecular and cortical bone health improved after loading in both the control and the irradiated experimental groups. Previous studies have also proven that mechanical loading improves bone health (12, 13). Therefore, radiation therapy does not impair the bone's ability to respond to mechanical loading, as the absolute increase in BV/TV was similar between groups. In late loading, the effect of mechanical loading appears to decrease. Although this is not completely comparable, since the mice differ in sensitivity, the loading was therefore higher in absolute terms in the older mice, requiring later loading to achieve the same effect on the bone. The reduced increase in BV/TV observed in the 12-week loading experiment may be partly explained by differences in skeletal maturity. Previous studies have shown that the anabolic response to mechanical loading is stronger in younger mice and gradually declines as the skeleton matures (59, 60). Mice in the early loading experiment were sacrificed at 14 weeks of age, whereas mice in the late loading experiment were 22 weeks old and therefore more skeletally mature. Both ages are after the growth spurt but are still considered young mice (59). This may explain the reduced bone-forming response observed at the later time point.

To investigate whether systemic differences in bone formation or resorption between control and irradiated mice could be detected, two markers, PINP and CTX-I, were measured. PINP showed a slightly significant increase at 12 weeks. Loading-induced bone formation, which may be further reduced after irradiation, thereby indicating greater bone formation in the irradiated mice. However, µCT results do not show greater bone formation in irradiated mice than in control mice. A difference in CTX-I was expected between control and irradiated mice, as irradiation is known to cause bone loss, and a previous study by Sághy T. et al. also noted an increase in CTX-I (14, 22). Although no differences were observed. ELISA tests provide a snapshot, so it is possible that the increased bone resorption had already occurred, as there is a clear decrease in the BV/TV in irradiated mice.

Several limitations of this study should be considered when interpreting the findings. A major limitation was the inability to fully optimize the 3D imaging workflow for reliable visualization of osteoclast and osteoblast populations within the bone microenvironment. Although tissue clearing and apoptotic cell detection were successfully achieved, high bone autofluorescence and insufficient performance of several bone-specific antibodies limited the ability to investigate potential *in vivo* interactions between apoptotic cells and bone-resident cells. Nevertheless, successful staining of cleaved caspase-3 and B220 confirmed that tissue preservation and antibody penetration were not universally impaired, indicating that the main challenges were likely marker-specific rather than due to overall tissue-processing failure.

An important strength of this study is the unilateral loading model, in which loaded and non-loaded limbs originated from the same animal. This approach minimizes inter-individual variability and ensures that both limbs are exposed to the same systemic environment, thereby enabling a more reliable assessment of local skeletal adaptations induced by loading. However, this experimental design also complicates the interpretation of systemic ELISA measurements and flow cytometry analysis, as circulating marker and cell levels reflect the combined effects of irradiation and loading and do not allow discrimination between local and systemic responses. In addition, no significant differences in circulating bone formation or resorption markers were observed. Since ELISA measurements provide only a single time-point snapshot of systemic marker levels, transient or temporally restricted changes in bone turnover may have occurred outside the selected time points and therefore remained undetected.

## CONCLUSION

In conclusion, this study successfully established a workflow for tissue clearing of irradiated bones. While tissue clearing and apoptotic cell detection were successfully achieved, further optimization of bone-specific immunostaining is required to reliably visualize osteoclasts and osteoblasts within bone tissue. In addition, this study demonstrated that irradiation combined with subsequent mechanical loading induces persistent alterations in bone, affecting both skeletal integrity and immune cell composition. It resulted in prolonged immune alterations, including changes in thymus and spleen weight, elevated BAFF levels, and increased B cell frequency at later time points, indicating sustained modulation of immune homeostasis following irradiation and mechanical loading. Despite radiation-induced bone loss, the skeleton retained its responsiveness to mechanical stimuli, with mechanical loading improving both trabecular and cortical bone parameters in control and irradiated mice. Altogether, these findings provide further insight into the long-term skeletal consequences of irradiation and highlight mechanical loading as a promising strategy to mitigate radiation-induced bone deterioration.

## REFERENCES

1. Chen H, Han Z, Luo Q, Wang Y, Li Q, Zhou L, et al. Radiotherapy modulates tumor cell fate decisions: a review. Radiat Oncol. 2022;17(1):196.
2. Zafar A, Khatoon S, Khan MJ, Abu J, Naeem A. Advancements and limitations in traditional anti-cancer therapies: a comprehensive review of surgery, chemotherapy, radiation therapy, and hormonal therapy. Discover Oncology. 2025;16(1):607.
3. Baskar R, Lee KA, Yeo R, Yeoh KW. Cancer and radiation therapy: current

advances and future directions. Int J Med Sci. 2012;9(3):193-9.
4. Johansson P, Kristjansdottir HL, Johansson H, Mellström D, Lewerin C. Increased risk of hip and major osteoporotic fractures in 8463 patients who have undergone stem cell transplantation, a Swedish population-based study. Osteoporos Int. 2024;35(10):1831-8.
5. Omurzakov A, Rampam S, Gonzalez MR, Lozano-Calderon SA. What is the incidence and non-union rate of radiation-associated fractures? – A systematic review of the literature. Radiotherapy and Oncology. 2025;202:110617.
6. Curi MM, Cardoso CL, de Lima HG, Kowalski LP, Martins MD. Histopathologic and Histomorphometric Analysis of Irradiation Injury in Bone and the Surrounding Soft Tissues of the Jaws. J Oral Maxillofac Surg. 2016;74(1):190-9.
7. Burr DB, Akkus O. Chapter 1 - Bone Morphology and Organization. In: Burr DB, Allen MR, editors. Basic and Applied Bone Biology. San Diego: Academic Press; 2014. p. 3-25.
8. Engdahl C. Arthritis and immune-mediated bone loss - role of estrogen signalling pathways: Kompendiet, Gothenburg; 2013.
9. Allen MR, Burr DB. Chapter 4 - Bone Modeling and Remodeling. In: Burr DB, Allen MR, editors. Basic and Applied Bone Biology. San Diego: Academic Press; 2014. p. 75-90.
10. Maciel GBM, Maciel RM, Danesi CC. Bone cells and their role in physiological remodeling. Molecular Biology Reports. 2023;50(3):2857-63.
11. Bellido T, Plotkin LI, Bruzzaniti A. Chapter 2 - Bone Cells. In: Burr DB, Allen MR, editors. Basic and Applied Bone Biology. San Diego: Academic Press; 2014. p. 27-45.
12. Liphardt AM, Windahl SH, Sehic E, Hannemann N, Gustafsson KL, Bozec A, et al. Changes in mechanical loading affect arthritis-induced bone loss in mice. Bone. 2020;131:115149.
13. Desai S, Wu J, Horkeby K, Norgård M, Ohlsson C, Windahl SH, et al. A COX-2 Inhibitor Does Not Interfere With the Bone-Protective Effects of Loading in Male Mice With Arthritis. JBMR Plus. 2023;7(7):e10751.
14. Sághy T, Gupta P, Horkeby K, Henning P, Ohlsson C, Corciulo C, et al. Disrupted bone microenvironment and immune recovery following total body irradiation in a murine model. Cell Death & Disease. 2025;17(1):122.
15. Wei F, Tuong ZK, Omer M, Ngo C, Asiatico J, Kinzel M, et al. A novel multifunctional radioprotective strategy using P7C3 as a countermeasure against ionizing radiation-induced bone loss. Bone Research. 2023;11(1):34.
16. Heylmann D, Ponath V, Kindler T, Kaina B. Comparison of DNA repair and radiosensitivity of different blood cell populations. Sci Rep. 2021;11(1):2478.
17. Paganetti H. A review on lymphocyte radiosensitivity and its impact on radiotherapy. Front Oncol. 2023;13:1201500.
18. Sazonova EV, Petrichuk SV, Kopeina GS, Zhivotovsky B. A link between mitotic defects and mitotic catastrophe: detection and cell fate. Biology Direct. 2021;16(1):25.
19. Vitale I, Galluzzi L, Castedo M, Kroemer G. Mitotic catastrophe: a mechanism for avoiding genomic instability. Nature Reviews Molecular Cell Biology. 2011;12(6):385-92.
20. Lloyd SA, Bandstra ER, Travis ND, Nelson GA, Bourland JD, Pecaut MJ, et al. Spaceflight-relevant types of ionizing radiation and cortical bone: Potential LET effect? Adv Space Res. 2008;42(12):1889-97.
21. Ott Susan M. Cortical or Trabecular Bone: What's the Difference? American Journal of Nephrology. 2018;47(6):373-5.
22. Berk L. The effects of high-dose radiation therapy on bone: a scoping review. Radiat Oncol J. 2024;42(2):95-103.
23. Mustafa M, Ahmad R, Tantry IQ, Ahmad W, Siddiqui S, Alam M, et al.

Apoptosis: A Comprehensive Overview of Signaling Pathways, Morphological Changes, and Physiological Significance and Therapeutic Implications. Cells. 2024;13(22):1838.
24. Savitskaya MA, Onishchenko GE. Mechanisms of apoptosis. Biochemistry (Moscow). 2015;80(11):1393-405.
25. Sheng YR, Hu WT, Chen S, Zhu XY. Efferocytosis by macrophages in physiological and pathological conditions: regulatory pathways and molecular mechanisms. Frontiers in Immunology. 2024;Volume 15 - 2024.
26. Gheibi Hayat SM, Bianconi V, Pirro M, Sahebkar A. Efferocytosis: molecular mechanisms and pathophysiological perspectives. Immunology & Cell Biology. 2019;97(2):124-33.
27. Moon B, Yang S, Moon H, Lee J, Park D. After cell death: the molecular machinery of efferocytosis. Experimental & Molecular Medicine. 2023;55(8):1644-51.
28. Batoon L, Hawse JR, McCauley LK, Weivoda MM, Roca H. Efferocytosis and Bone Dynamics. Current Osteoporosis Reports. 2024;22(5):471-82.
29. Harre U, Keppeler H, Ipseiz N, Derer A, Poller K, Aigner M, et al. Moonlighting osteoclasts as undertakers of apoptotic cells. Autoimmunity. 2012;45(8):612-9.
30. Batoon L, Koh AJ, Kannan R, McCauley LK, Roca H. Caspase-9 driven murine model of selective cell apoptosis and efferocytosis. Cell Death Dis. 2023;14(1):58.
31. Jobling MF, Mott JD, Finnegan MT, Jurukovski V, Erickson AC, Walian PJ, et al. Isoform-Specific Activation of Latent Transforming Growth Factor β (LTGF-β) by Reactive Oxygen Species. Radiation Research. 2006;166(6):839-48.
32. McDonald MM, Kim AS, Mulholland BS, Rauner M. New Insights Into Osteoclast Biology. JBMR Plus. 2021;5(9):e10539.
33. Yahara Y, Barrientos T, Tang YJ, Puviindran V, Nadesan P, Zhang H, et al. Erythromyeloid progenitors give rise to a population of osteoclasts that contribute to bone homeostasis and repair. Nat Cell Biol. 2020;22(1):49-59.
34. Kong YY, Yoshida H, Sarosi I, Tan HL, Timms E, Capparelli C, et al. OPGL is a key regulator of osteoclastogenesis, lymphocyte development and lymph-node organogenesis. Nature. 1999;397(6717):315-23.
35. Li Y, Toraldo G, Li A, Yang X, Zhang H, Qian WP, et al. B cells and T cells are critical for the preservation of bone homeostasis and attainment of peak bone mass in vivo. Blood. 2007;109(9):3839-48.
36. Jin M, Nguyen JD, Weber SJ, Mejias-Aponte CA, Madangopal R, Golden SA. SMART: An Open-Source Extension of WholeBrain for Intact Mouse Brain Registration and Segmentation. eneuro. 2022;9(3):ENEURO.0482-21.2022.
37. Zou Q, Hong W, Zhou Y, Ding Q, Wang J, Jin W, et al. Bone marrow stem cell dysfunction in radiation-induced abscopal bone loss. J Orthop Surg Res. 2016;11:3.
38. Guliyeva G, Takile FNF, Stallfort V, Derer A, Frey B, Gupta P, et al. AnnexinA1-Dectin 1 axis is a key regulator of osteoclastogenesis underlying irradiation induced bone loss in male mice. J Bone Miner Res. 2026.
39. Shrirao AB, Schloss RS, Fritz Z, Shrirao MV, Rosen R, Yarmush ML. Autofluorescence of blood and its application in biomedical and clinical research. Biotechnol Bioeng. 2021;118(12):4550-76.
40. Fauch L, Palander A, Dekker H, Schulten EA, Koistinen A, Kullaa A, et al. Narrowband-autofluorescence imaging for bone analysis. Biomed Opt Express. 2019;10(5):2367-82.
41. Dholakia U, Clark-Price SC, Keating SCJ, Stern AW. Anesthetic effects and body weight changes associated with ketamine-xylazine-lidocaine administered to CD-1 mice. PLoS One. 2017;12(9):e0184911.
42. Welberg LA, Kinkead B, Thrivikraman K, Huerkamp MJ, Nemeroff CB, Plotsky PM. Ketamine-xylazine-

acepromazine anesthesia and postoperative recovery in rats. J Am Assoc Lab Anim Sci. 2006;45(2):13-20.
43. Calvez J, Fromentin G, Nadkarni N, Darcel N, Even P, Tomé D, et al. Inhibition of food intake induced by acute stress in rats is due to satiation effects. Physiol Behav. 2011;104(5):675-83.
44. Maniam J, Morris MJ. The link between stress and feeding behaviour. Neuropharmacology. 2012;63(1):97-110.
45. Marci R, Mallozzi M, Di Benedetto L, Schimberni M, Mossa S, Soave I, et al. Radiations and female fertility. Reprod Biol Endocrinol. 2018;16(1):112.
46. Teh WT, Stern C, Chander S, Hickey M. The impact of uterine radiation on subsequent fertility and pregnancy outcomes. Biomed Res Int. 2014;2014:482968.
47. Fredrickson GG, Basch RS. Early thymic regeneration after irradiation. Developmental & Comparative Immunology. 1994;18(3):251-63.
48. Majumdar S, Nandi D. Thymic Atrophy: Experimental Studies and Therapeutic Interventions. Scandinavian Journal of Immunology. 2018;87(1):4-14.
49. Liang Z, Dong X, Zhang Z, Zhang Q, Zhao Y. Age-related thymic involution: Mechanisms and functional impact. Aging Cell. 2022;21(8):e13671.
50. Këpuska Z, Sempowski G. Mechanisms of thymic recovery and T cell reconstitution following sublethal ionizing radiation (104.21). The Journal of Immunology. 2011;186(1_Supplement):104.21-.21.
51. Mohtashami M, Li YR, Lee CR, Zúñiga-Pflücker JC. Thymus Reconstitution in Young and Aged Mice Is Facilitated by In Vitro-Generated Progenitor T Cells. Front Immunol. 2022;13:926773.
52. Zlotoff DA, Zhang SL, De Obaldia ME, Hess PR, Todd SP, Logan TD, et al. Delivery of progenitors to the thymus limits T-lineage reconstitution after bone marrow transplantation. Blood. 2011;118(7):1962-70.
53. Velardi E, Tsai JJ, van den Brink MRM. T cell regeneration after immunological injury. Nat Rev Immunol. 2021;21(5):277-91.
54. Almeida AR, Borghans JA, Freitas AA. T cell homeostasis: thymus regeneration and peripheral T cell restoration in mice with a reduced fraction of competent precursors. J Exp Med. 2001;194(5):591-9.
55. Rittase WB, Slaven JE, Suzuki YJ, Muir JM, Lee S-H, Rusnak M, et al. Iron Deposition and Ferroptosis in the Spleen in a Murine Model of Acute Radiation Syndrome. International Journal of Molecular Sciences. 2022;23(19):11029.
56. Schweighoffer E, Tybulewicz VL. BAFF signaling in health and disease. Curr Opin Immunol. 2021;71:124-31.
57. Pietras Eric M, Reynaud D, Kang Y-A, Carlin D, Calero-Nieto Fernando J, Leavitt Andrew D, et al. Functionally Distinct Subsets of Lineage-Biased Multipotent Progenitors Control Blood Production in Normal and Regenerative Conditions. Cell Stem Cell. 2015;17(1):35-46.
58. Lustberg MB. Management of neutropenia in cancer patients. Clin Adv Hematol Oncol. 2012;10(12):825-6.
59. Kendall JJ, Kuhn GA, Schulte FA, Müller R. How bones learn to listen: In vivo models for investigating mechanosensitivity at bony interfaces in the ageing mouse. Annals of Anatomy - Anatomischer Anzeiger. 2026:152838.
60. Chen Y, Klein-Nulend J, Bravenboer N. Ageing-Related Changes in Ultrastructural Bone Matrix Composition and Osteocyte Mechanosensitivity. Curr Osteoporos Rep. 2025;23(1):35.

*Acknowledgments* – I would like to express my sincere gratitude to Cecilia Engdahl for welcoming me into her research team and providing me with this valuable and enriching opportunity. I am especially thankful for her supervision, guidance, and support throughout my project, as well as for always being available to answer my questions and share her expertise. I would also like to thank Vilma Enlund for the

opportunity to contribute to her project, which allowed me to gain additional hands-on experience and broaden my research skills. Furthermore, I would like to thank Xin Tian from Chagin's group for teaching me the staining protocols and providing valuable assistance throughout the laboratory work. Finally, I am grateful to everyone who supports and encourages me, and to those who create a welcoming and inspiring research environment.

*Author contributions* – CE conceived and designed the research. CE, BVDB, KH and VE performed experiments. XT assisted BVDB during the staining procedures. BVDB performed the data analysis and this master's thesis. BVDB and CE carefully edited the manuscript.

*Note* - This thesis is grammatically supported by Gen AI.

## SUPPORTING INFORMATION

**Suppl table 1. Stainings FACS**

| Antibody | Dilution | Supplier, Reference |
|---|---|---|
| APC anti-mouse F4/80 Antibody | 1/100 | BioLegend, AB_893481 |
| APC-Cy™7 Rat Anti-CD11b | 1/100 | BD Pharmingen™, AB_396772 |
| Ly-6G/Ly-6C Monoclonal Antibody (RB6-8C5), PE | 1/100 | eBioscience™, 12-5931-83 |
| PE/Cyanine7 anti-mouse CD3 Antibody | 1/100 | BioLegend, AB_1732057 |
| FITC Rat Anti-Mouse CD19 | 1/100 | BD Pharmingen™, AB_396681 |

**Suppl table 2. Primary and secondary antibodies 2D and 3D imaging**

| Primary antibody | Dilution | Supplier, Reference |
|---|---|---|
| Anti-Cathepsin K antibody | 1/100 | Abcam, ab19027 |
| Biotin anti-mouse/human CD45R/B220 Antibody | 1/100 | BioLegend, 103204 |
| Anti-Tartrate Resistant Acid Phosphatase antibody [ACP5/1070] | 1/400 | Abcam, ab216025 |
| Anti-Tartrate Resistant Acid Phosphatase antibody | 1/400 | Abcam, ab185716 |
| Human/Mouse NCAM-1/CD56 Antibody | 1/400 | R&D systems, AF2408 |
| Anti-Sp7 / Osterix antibody | 1/400 | Abcam, ab22552 |
| Osterix/Sp7 Antibody | 1/400 | R&D systems, FAB7547A |
| Cleaved Caspase-3 (Asp175) antibody | 1/400 | Cell Signaling, 9661 |
| **Secondary antibody** | **Dilution** | **Supplier, Reference** |
| Donkey anti-Mouse IgG, Alexa Fluor™ 546 | 1/400 | Invitrogen, A10036 |
| Donkey anti-Mouse IgG, Alexa Fluor™ 790 | 1/400 | Invitrogen, A11371 |
| Donkey anti-Goat IgG, Alexa Fluor™ 546 | 1/400 | Invitrogen, A-11056 |
| Donkey anti-Goat IgG, Alexa Fluor™ Plus 647 | 1/400 | Invitrogen, A32849TR |
| Donkey anti-Rabbit IgG, Alexa Fluor™ 647 | 1/400 | Invitrogen, A-31573 |
| Donkey anti-Rabbit IgG, DyLight™ 488 | 1/400 | Invitrogen, SA5-10038 |
| Donkey anti-Rat IgG, Alexa Fluor™ 647 | 1/400 | Invitrogen, A78947 |

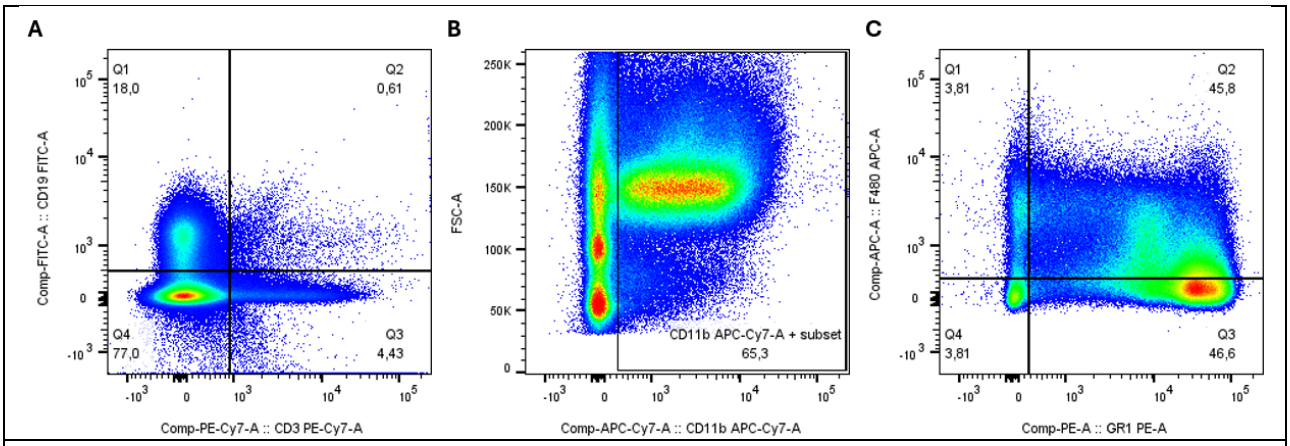


**Suppl fig. 1: FMO-based gating strategy for flow cytometry analysis. A** Representative gating strategy for the identification of B cells ($CD19^+$) and T cells ($CD3^+$). Gates were established using fluorescence minus one (FMO) controls and applied to singlet, viable cells. **B** Representative gating strategy for the identification of $CD11b^+$ myeloid cells within the $CD3^-$ population. **C** Representative gating strategy for the identification of $GR1^+$ and $F4/80^+$ cell populations within the $CD3^-CD11b^+$ population.

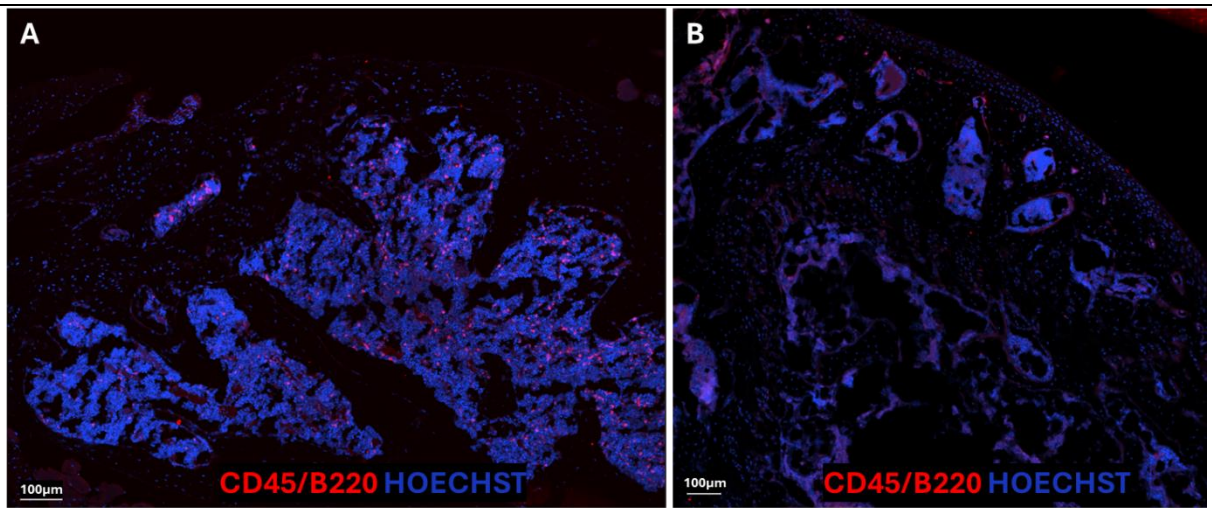


**Supplementary figure 2: 2D images of the tibial growth plate 2 weeks after total body irradiation**. Stained for CD45/B220 (B cells, red), and Hoechst (nucleus, blue). **A** Control bone. **B** Irradiated bone.

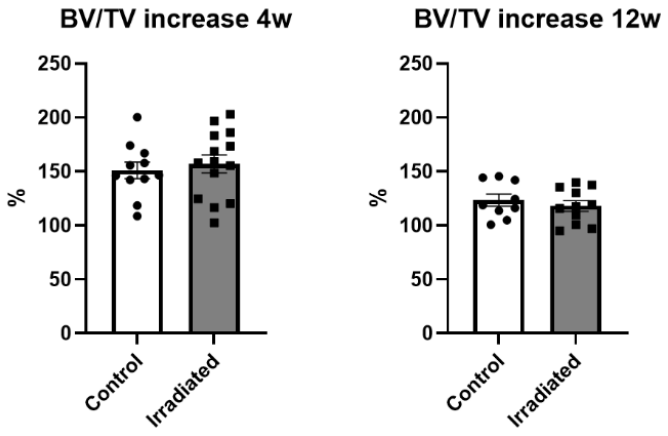


**Supplementary figure 3: Absolute bone volume per tissue volume (BV/TV) increase at 4 weeks and 12 weeks after mechanical loading.** Micro-computed tomography (µCT) was used to analyze trabecular BV/TV in the tibia and to calculate the absolute BV/TV increase at both timepoints in both experimental groups. Statistical analysis involved a two-sided unpaired t-test with Welch's correction. Data are presented as mean (n = 9-14) ± SD.